

**Stress Changes on the Garlock fault during and after the  
2019 Ridgecrest Earthquake Sequence**

1. **Marlon D. Ramos**<sub>1</sub>      ramosmd@umich.edu
2. **Jing Ci Neo**<sub>1</sub>      neoj@umich.edu
3. **Prithvi Thakur**<sub>1</sub>      prith@umich.edu
4. **Yihe Huang**<sub>1</sub>      yiheh@umich.edu
5. **Shengji Wei**<sub>2</sub>      shjwei@ntu.edu.sg

1. **University of Michigan, Department of Earth and Environmental Sciences**
2. **Nanyang Technological University of Singapore, Asian School of the Environment**

Preprint submitted to EarthArXiv

1  
2  
3  
4  
5  
6  
7  
8  
9  
10  
11  
12  
13  
14  
15  
16  
17  
18  
19  
20  
21  
22  
23  
24  
25  
26  
27  
28  
29  
30  
31  
32  
33  
34  
35  
36  
37  
38  
39  
40  
41  
42  
43  
44  
45  
46

47 **Abstract**

48       The recent 2019 Ridgecrest earthquake sequence in Southern California jostled the  
49 seismological community by revealing a complex and cascading foreshock series that culminated  
50 in a M7.1 mainshock. But the central Garlock fault, despite being located immediately south of  
51 this sequence, did not coseismically fail. Instead, the Garlock fault underwent post-seismic creep  
52 and exhibited a sizeable earthquake swarm. The dynamic details of the rupture process during the  
53 mainshock is largely unknown, as is the amount of stress needed to bring the Garlock fault to  
54 failure. We present an integrated view of how stresses changed on the Garlock fault during and  
55 after the mainshock using a combination of tools including kinematic slip inversion, Coulomb  
56 stress change, and dynamic rupture modeling. We show that positive Coulomb stress changes  
57 cannot easily explain observed aftershock patterns on the western section of the Garlock fault, but  
58 are consistent with where creep was documented on the central Garlock fault section. Our dynamic  
59 model is able to reproduce the main slip asperities and kinematically estimated rupture speeds ( $\leq$   
60 2 km/s) during the mainshock, and suggests the temporal changes in normal and shear stress on  
61 the Garlock fault were greatest near the end of rupture. The largest static and dynamic stress  
62 changes on the Garlock fault we observe from our dynamic model coincide with the creeping  
63 region, suggesting that positive stress perturbations could have caused this during or after the  
64 mainshock rupture. This analysis of near-field stress change evolution gives insight into how the  
65 Ridgecrest sequence influenced the local stress field of the northernmost Eastern California Shear  
66 Zone.

67 **Introduction**

68       The 2019 Ridgecrest earthquake sequence involved the rupture of a left-lateral M6.4  
69 foreshock that occurred on July 4, and a right-lateral M7.1 mainshock that occurred on July 6 and  
70 initiated approximately 13 km northwest of the foreshock epicenter (Fig. 1). This sequence was  
71 characterized by the activation of multiple orthogonal fault segments that are collectively referred  
72 to as the Little Lake fault zone (Llfz). Coseismic rupture of these faults continues to produce  
73 aftershocks, but it did not influence the adjacent left-lateral Garlock fault to fail. Instead, this  
74 sequence caused as much as three centimeters of surface creep on the Garlock fault that has been  
75 detected geodetically (Barnhart et al., 2019; Ross et al., 2019).

76       Several kinematic slip models have been developed to estimate the evolution of slip and  
77 rupture propagation during this highly complex sequence (Barnhart et al., 2019; Goldberg et al.,

78 2019; Liu et al., 2019; Ross et al., 2019). These models are consistent in the respect that a majority  
79 of foreshock and mainshock slip is limited to the upper 10 km depth. Positive stress change  
80 amplitudes ( $\sim 0.5$  MPa) are suggested from static Coulomb modeling and generally coincide with  
81 the  $\sim 25$  km long region of creep on the central Garlock fault segment (Barnhart et al., 2019). But  
82 the dynamic details of rupture and how stresses were mediated by the seismic wavefield remains  
83 hazy. The Garlock fault was apparently not near critical failure, or else we would have observed  
84 coseismic rupture there as well; this implies that the stress perturbations were unable to bring shear  
85 stresses to overcome the static Garlock fault strength.

86       When the Garlock fault will slip again is a major unknown. The Garlock fault extends for  
87  $\sim 260$  km and is geometrically segmented into western, central, and eastern sections that are  
88 characterized by variations in geologic slip-rate and recurrence interval (Davis and Burchfiel,  
89 1973; Hill et al., 1953, McGill and Sieh, 1991; Fig. 1). Astiz and Allen (1983) analyzed historical  
90 seismicity on this fault and hypothesized that a rupture on the eastern Garlock segment may be  
91 more likely given its apparent seismic gap, though both the central and western sections can  
92 independently support  $\sim M7$  earthquakes. Paleoseismic evidence suggests historic, non-periodic  
93 surface rupture for the central Garlock segment (Dawson et al., 2003), which is the closest segment  
94 to the Ridgecrest sequence. Portions of this segment also experienced a swarm of low-magnitude  
95 earthquakes ( $ML < 3.2$ ; Ross et al., 2019) and underwent creep. How the strain accumulation  
96 budget of the central Garlock fault was influenced by the recent Ridgecrest sequence is enigmatic  
97 and warrants further scrutiny for seismic hazard analysis. A spatial separation between the  
98 mainshock and Garlock fault planes is furthermore subject to uncertainty, as is the possibility of  
99 rupture branching from a segment of the Garlock fault onto an adjacent segment or to the San  
100 Andreas fault during a future earthquake. In particular, the central and western segments have co-  
101 ruptured within the last 10 kya, despite a step-over structure in between them (Madugo et al.,  
102 2012). Assessing the possibility of how close the Garlock fault is to failure depends on both the  
103 static and dynamic stress perturbations from the Ridgecrest sequence.

104       We aim to present a physically consistent picture of the stress interaction vis-à-vis the  
105 Garlock fault during and after the Ridgecrest sequence. We draw from updated kinematic  
106 inversion results that utilizes teleseismic and near-field strong ground-motion recordings to  
107 independently constrain the fault slip amplitude, extent and rupture initiation locations of the  
108 foreshocks and M7.1 mainshock. This is then used to inform our static Coulomb stress analysis

109 and dynamic rupture modeling efforts. We also discuss how our dynamic rupture model is  
110 consistent with theoretical predictions that suggest the Garlock fault was in a dynamically  
111 unfavorable set of conditions to co-rupture with the mainshock. Our analysis illustrates that both  
112 normal and shear stress changes were highest on the Garlock fault at the end of mainshock rupture,  
113 and could have been responsible for the observed geodetic creep.

## 114 **Methodology**

### 115 *Kinematic Slip Inversion*

116 We use a joint slip-inversion model that is based on static GPS, teleseismic and local  
117 strong-ground motion datasets (Ji et al., 2002). The M6.4 foreshock and the M7.1 mainshock are  
118 modeled with two and one fault segments, respectively. Here, the mainshock hypocenter has been  
119 relocated to a depth of 3 km by the arrival times of nearby strong motion and broadband seismic  
120 stations. Fault plane geometries roughly follow the USGS surface mapping and seismicity (Fig. 2)  
121 and the fault parameters and hypocenters of both earthquakes are summarized in Table 1. We note  
122 that the M7.1 mainshock ruptured bilaterally with a majority of slip concentrated within the upper  
123 10 km and a peak slip amplitude of 4.7 m located ~10 km NW of the hypocenter (Fig. 2). On the  
124 other hand, peak slip resolved for the foreshock is lower (1.3 m) and occurred mostly on the NE-  
125 SW striking fault plane (Supplemental Fig 2). We use the slip inversion result for the mainshock  
126 fault plane as input to our Coulomb stress change modeling.

127 We also compare our slip inversion results to those from other studies of the Ridgecrest  
128 mainshock slip. We utilize seismic and GPS datasets to constrain the slip which is similar to the  
129 approach by Liu et al., (2019). In contrast, other studies make use of a combination of high-rate  
130 GPS and Interferometric Synthetic Aperture Radar imagery (InSAR, Goldberg et al., 2019; Ross  
131 et al., 2019) or both InSAR and optimal image-tracking data (Barnhart et al., 2019). The details of  
132 slip distribution and the relative locations of maximum slip vary between different studies. The  
133 maximum slip is mostly shallower than (Barnhart et al., 2019), to the northwest of (Liu et al.,  
134 2019), or slightly deeper (Ross et al., 2019) than the hypocenter location used in their inversion.  
135 The kinematic slip inversion we present resolves two primary slip patches (i.e., Fig. 2), which have  
136 similar slip amplitudes (4.7 m and 2.5 m) and slip patch locations (northwest and southeast of  
137 hypocenter) to the Barnhart et al., (2019) and Liu et al., (2019) inversion results. Overall, our slip  
138 distribution is consistent with published models, characterized by bilateral rupture propagation and  
139 a shallow (< 10 km) slip distribution.

140 *Static Model: Coulomb Stress-Change*

141         Static stress changes are the final changes in the normal and shear stresses on the fault in  
142 response to slip after all seismic waves have propagated through. Such stress changes during the  
143 foreshock and mainshock of the Ridgecrest sequence have triggered thousands of aftershocks  
144 (Ross et al., 2019). Coseismic stress changes have also been known to trigger or to reduce creep  
145 after the earthquake (e.g., Allen et al., 1972, Bodin et al., 1994, Lienkaemper et al., 1997). Barnhart  
146 et al. (2019) observed that an increase in the Coulomb stress change from the Ridgecrest  
147 earthquake was correlated with the surface deformation after the earthquake. Studies have also  
148 suggested that the M6.4 foreshock and other large foreshocks promoted the rupture of the  
149 mainshock (Barnhart et al., 2019; Goldberg et al., 2019).

150         To assess static stress changes, we calculate the Coulomb stress change (Lin and Stein  
151 2004; Toda et al. 2005), denoted by  $\Delta CFS$ , caused by the foreshock on the mainshock and separate  
152 the contribution of stress change from each of the two foreshock fault planes. We also calculate  
153 the  $\Delta CFS$  due to mainshock slip on the Garlock fault. We represent the Garlock fault geometry as  
154 a plane with a strike, dip and rake of 70, 90, and 0 degrees, respectively. The strike of the Garlock  
155 fault varies from 68° in the east to 84° in the west (Fig. 6), but we use 70° for the receiver fault as  
156 it is closest to the strike of the western Garlock fault segment where the cluster of aftershocks  
157 occurred. We use a friction coefficient of 0.6 and a depth of 5 km in both cases. To address  
158 uncertainty in static friction level and hypocenter depth, we also examine how varying these  
159 parameters influences our results. We compare the results from friction coefficients of 0.2, 0.4 and  
160 0.6, and at 5 km depth, where peak slip occurred, and at 10 km depth, where the asperity with most  
161 slip extends.

162 *Dynamic Model: Initial Conditions and Constraints*

163         We model the mainshock fault plane as a 100-km, planar 2-D crack embedded in a  
164 homogeneous, isotropic, and linearly elastic medium with a shear-wave speed of 3.2 km/s. The  
165 model domain is composed of rectangular quadrilateral elements enclosed on all sides by  
166 absorbing boundaries (Supplementary Fig. S1). We choose a finite element size of 600-m with  
167 four Gauss-Lobatto-Legendre nodes (NGLL) to resolve dynamic rupture propagation at seismic  
168 frequencies up to 1 Hz for consistency with that resolved by the strong-motion dataset.

169         We select the linear slip-weakening friction law to control fault slip evolution and utilize  
170 the 2-D spectral element code SEM2DPACK to solve for dynamic rupture propagation (Ampuero,

171 2009, <https://sourceforge.net/projects/sem2d/>). The critical-slip distance ( $D_c$ ) is 0.3 m, which is  
172 constant along the fault (except for  $\sim 15$  km around the nucleation region) and is within the  
173 plausible range of previous slip-weakening dynamic rupture simulations for other crustal  
174 earthquakes of comparable magnitude and rupture dimension (e.g., Ma and Archuleta, 2006; Tinti  
175 et al., 2009). If dynamic friction ( $\mu_d$ ) is below the static friction ( $\mu_s$ ) level, then the fault  
176 experiences a strength-drop during coseismic rupture and its frictional behavior is slip-weakening;  
177 conversely, if the dynamic friction is greater than static friction, there is no work available to grow  
178 the propagating shear crack and the frictional behavior is slip-strengthening. The static friction  
179 coefficient is everywhere 0.5 along the fault. The fault is slip-weakening ( $\mu_d = 0.1$ ) along the  
180 central 70 km segment (35 km southeast and northwest of hypocenter) and slip-strengthening ( $\mu_d =$   
181 0.7) everywhere else in order to prohibit rupture from breaking the entire fault.

182         Given that we represent a strike-slip fault as a Mode II in-plane crack, our stress and friction  
183 conditions are relative to a region on the mainshock fault plane at depth. Our model aims to  
184 reproduce the rupture propagation along the section of the fault that crosses through the main slip  
185 asperity imaged in the kinematic inversion (Fig. 6). Effective normal stress is set to a constant  
186 level of 50 MPa that is consistent with elevated pore-pressure levels in the middle of permeable  
187 fault zones (Rice, 1992).

188         The initial shear stress distribution is a critical ingredient for any dynamic earthquake  
189 rupture model and determines the dynamic stress drop which in turn governs slip amplitude. We  
190 first calculate the static stress drop due to fault slip given by the kinematic inversion using a  
191 computationally efficient algorithm (Fig. 3; Ripperger and Mai, 2004). Earthquakes can exhibit  
192 total or near-total stress-drop due to strong dynamic weakening (e.g., Noda and Lapusta, 2013;  
193 Brodsky et al., 2020), meaning that the final shear stress on the fault after an earthquake is at or  
194 very near its dynamic fault strength level (the product of effective normal stress and dynamic  
195 friction). We make this assumption to calculate our initial shear stress by adding the static stress  
196 drop to the dynamic fault strength (Fig. 6).

197         Rupture is artificially nucleated in the middle of the fault using the time-weakening method  
198 (Andrews, 1985). This technique requires twice the critical half-crack length ( $2L_c$ ), an effective  
199 friction level ( $\mu_o$ ), and a weakening time scale ( $T_c$ ) after which the prescribed nucleation is turned  
200 off and rupture spontaneously evolves according to the non-linear interaction between fault

201 strengths and stresses. Given the friction law parameters we assume for Mode II rupture in an  
202 elastic domain,  $2L_c$  is given by

$$203 \quad 2L_c = \frac{2}{1-\nu} \frac{G}{\pi} \frac{\tau_s - \tau_d}{(\tau_o - \tau_d)^2} D_c \quad (1)$$

204 where  $G$  is the shear modulus (30 GPa),  $\nu$  is Poisson's ratio,  $\tau_s$  is the static fault strength,  
205  $\tau_d$  is the dynamic fault strength,  $\tau_o$  is the initial shear stress, and  $\mu_o$  is the effective friction  
206 coefficient calculated as the ratio between initial shear and effective normal stress amplitudes at  
207 the hypocenter. We determined that  $2L_c$  of 2 km,  $\mu_o$  of  $\sim 0.1$ , and  $T_c$  of 10 seconds are necessary  
208 to nucleate and sustain spontaneous rupture.

## 209 **Results**

### 210 *Static Stress Change*

211 We find the foreshock increased the  $\Delta CFS$  near the edges of the foreshock faults, especially  
212 at the intersection of Plane 2 and mainshock fault, but our relocated mainshock hypocenter is  
213 located in a region of slightly decreased  $\Delta CFS$  (Fig. 4a, Supplemental Fig. S3). However, this  
214 result depends on the method used to locate the mainshock hypocenter and its uncertainty. For  
215 example, the ANSS hypocenter is closer to ours but at twice the depth, while the hypocenter  
216 resolved by Ross et al. (2019) is much closer to the foreshock hypocenter but at twice the depth as  
217 well. The hypocenters estimated by the ANSS catalog and by Ross et al. (2019) are located near  
218 the edges of different regions of positive  $\Delta CFS$ . We also calculated the  $\Delta CFS$  from both foreshock  
219 planes separately (Fig. 4b, c). We denote the foreshock fault parallel to the main fault as Plane 1  
220 and the NE-SW striking cross-fault as Plane 2. Plane 2 has a much larger slip compared to Plane  
221 1, with almost twice the peak slip. However, Plane 1 causes larger Coulomb stress change on the  
222 mainshock fault compared to Plane 2, as Plane 1 is closer.

223 We further calculate the  $\Delta CFS$  on the Garlock fault due to mainshock slip and assess the  
224 effect of various friction coefficients and depths on our results. Overall, we find that the friction  
225 coefficient has a relatively small (i.e., a difference within  $\sim 0.1$  MPa) impact on our  $\Delta CFS$  results  
226 (Fig. 5). Larger friction coefficients increase the  $\Delta CFS$  amplitude and changes its distribution  
227 slightly (Fig. 5). This is similar to Barnhart et al. (2019), where they found that their results are  
228 consistent for all friction coefficients that they tested. Changing the depth from 5 km to 10 km  
229 increases the  $\Delta CFS$  amplitude and decreases the extent of the region of positive  $\Delta CFS$  on the  
230 Garlock fault sharply. The amplitude difference is because the largest portion of mainshock slip  
231

232 extends to about 10 km depth, and the change in slip at this depth produces a larger  $\Delta CFS$  than at  
233 5 km depth. The region of positive  $\Delta CFS$  in proximity to the creeping section of the Garlock fault  
234 is most consistent in spatial extent with that of Barnhart et al. (2019) when we use a friction  
235 coefficient of 0.2 and a depth of 5 km. Lastly, we find that the cluster of aftershocks on the Garlock  
236 fault are unlikely to be simply explained by Coulomb static stress change from the mainshock as  
237 the value of the stress change can be small and even negative (Fig. 5).

### 238 *Dynamic Earthquake Rupture model*

239 Our first goal is to explain the kinematic fault slip distribution using rupture dynamics. We  
240 seek to reproduce the two primary patches of 2.5 m and 4.7 m slip southeast and northwest of the  
241 hypocenter, respectively, (Fig. 3; 7a). We show the rupture history until 35 seconds to highlight  
242 the arrest of both the northwest and southeast rupture fronts (Fig. 7).

243 The initial conditions and friction parameters outlined in the methods section gives a good  
244 agreement between the kinematically imaged and dynamically modeled slip distributions. The  
245 exception is the region near the hypocenter, where the dynamic rupture model overpredicts the  
246 kinematic slip amplitude by  $\sim 0.8$  meters (Fig. 7a). This is most likely due to our time-weakening  
247 nucleation procedure, but is probably within the uncertainty of the true fault slip resolved by the  
248 kinematic inversion. The distribution in dynamic stress drop is positive where higher slip is  
249 concentrated, and negative in a small region southeast of the hypocenter and where we impose  
250 slip-strengthening frictional behavior at the ends of the fault (Fig. 7b).

251 The bilateral mainshock dynamic rupture is overall heterogeneous and spatiotemporally  
252 complex (Fig. 7c). There are three major asperities (i.e., relatively high dynamic stress-drop  
253 regions) that contribute to several rupture-front accelerations (Fig. 7b, c). The model shows a slow  
254 ( $< 1$  km/s) rupture front propagating to the southeast for the first 5 seconds after nucleation ceases;  
255 this southeast rupture front then accelerates to  $\sim 1.3$  km/s before decelerating and arresting at 28  
256 seconds (Figure 7c). In contrast, the northwest rupture front propagates at a more uniform speed  
257 ( $\sim 2.1$  km/s) before decelerating and stopping at  $\sim 25$  seconds. These rupture speeds are consistent  
258 with recent kinematic models that prescribe a constant sub-Rayleigh mainshock rupture speed  
259 (Goldberg et al., 2019; Liu et al., 2019; Ross et al., 2019). Rupture speed depends on how much  
260 total elastic work is partitioned into radiated or fracture energy during the faulting process. Slower  
261 ruptures (as observed during the Ridgecrest sequence) may be due to a relatively high fracture  
262 energy consumed on the fault, consistent with the hypothesis that the Llfz is less compliant and



263 more energy was needed to break multiple fault segments (Goldberg et al., 2019; Liu et al., 2019;  
264 Perrin et al., 2016). Our dynamic model shows that the mainshock rupture fronts do not exhibit  
265 slip-rate amplitudes above 4 m/s and propagate at well below the Rayleigh wave speed.

#### 266 *Temporal Stress Changes on the Garlock fault*

267 Using our dynamic rupture model, we investigate the stress contributions to a section of  
268 the central Garlock fault during and after the Ridgecrest mainshock. Note that given the  
269 limitation of our modeling domain, we cannot assess far-field dynamic stress contributions from  
270 surface-wave amplitude changes. We instead focus on how the initial peak stresses carried by  
271 near-field seismic waves impacted the Garlock fault during coseismic rupture.

272 The 2-D stress tensor in our model is for an isotropic body and yields three unique  
273 components:  $\sigma_{xx}$ ,  $\sigma_{yy}$ , and  $\sigma_{xy}$ . Only one component of the normal stress ( $\sigma_{yy}$ ) and the shear stress  
274 ( $\sigma_{xy}$ ) are important to be considered further in our analysis. If we place the strike of the mainshock  
275 fault plane on an east-west coordinate system, the angle between the mainshock and Garlock fault  
276 planes (measured clockwise) is approximately 110 degrees (Fig. 1a). We therefore applied a  
277 rotation of the stress field at a particular instant in time to represent the stress perturbation the  
278 mainshock imparts to the Garlock fault (Fig. 8; see Supplemental Information). When this rotation  
279 is performed at the final time-step, the rotated stress field is equivalent to the static stress change  
280 on the Garlock fault. We observe an abrupt transition from negative to positive normal static stress  
281 change as one crosses the intersection of the strike of the mainshock fault plane (Fig. 8a). The  
282 shear stress change is slightly more complex with an asymmetric stress amplitude distribution  
283 across the fault, but shows a very pronounced region of positive stress change that generally  
284 coincides with the ~25-km long section of the central Garlock fault that underwent creep (Fig. 8b;  
285 Barnhart et al., 2019; Xu et al., 2019). To confirm our static stress change analysis from the  
286 dynamic model, we compare it to our  $\Delta CFS$  calculation and find that its orientation and amplitude  
287 are consistent (Supplemental Fig. S4).

288 We also calculate the temporal stress change on the central Garlock fault segment during  
289 the Ridgecrest mainshock. We select one point near the creeping region on the Garlock fault (-60  
290 km, -10 km; Fig. 9, 10) to show how normal and shear stresses change during mainshock rupture.  
291 While propagation spontaneously arrests at near ~28 seconds towards the southeast, we simulate  
292 rupture until 100 seconds to make sure stress changes relax to constant levels, which are attained

293 at 60 seconds (Fig. 11). This section of the central Garlock fault begins to experience a positive  
294 normal stress change near 17.5 seconds (Fig. 9). During the main portion of coseismic rupture,  
295 normal stress changes reach their maximum of  $\sim 0.3$  MPa at 32 seconds (Fig. 9f, 11a). In contrast,  
296 positive shear stress changes arrive at the Garlock fault in three distinct pulses (e.g., Fig. 10f, 11a).  
297 Two of these positive shear stress change pulses arrive after the largest change in normal stress  
298 change and continue to be above the normal stress change amplitude for the remainder of our  
299 simulation (Fig. 10, 11a). The extrema of the normal and shear stress change amplitudes are  
300 symmetric through time due to the alternating arrivals of compressional (P) and shear (SV) wave  
301 motions.

### 302 **Discussion and Conclusion**

303 We show that stress changes during and after the Ridgecrest foreshocks and mainshock  
304 may have influenced post-seismic creep on the central Garlock fault segment and brought certain  
305 regions closer to coseismic failure. Our results also shed light on the temporal stress evolution on  
306 the Garlock fault due to source dynamics. Because both normal and shear stresses vary during  
307 coseismic rupture, evaluating their respective contribution is of critical importance to identifying  
308 periods when stresses changes may have been favorable to engender the observed post-seismic  
309 creep.

310 The Coulomb stress change results show that positive static stress changes were  
311 experienced on the central Garlock fault due to mainshock slip (Fig. 4 and 5) and are coincident  
312 with previously documented fault creep (Barnhart et al., 2019; Ross et al., 2019; Xu et al., 2020).  
313 Among Coulomb stress changes calculated for different friction levels and depths, in only one case  
314 (i.e., friction level of 0.6) is the positive static stress change seen to coincide with the section of  
315 the Garlock fault that experienced a sizeable aftershock swarm (Fig. 5). This may indicate that  
316 other post-seismic relaxation processes were at play to produce this aftershock pattern. When we  
317 assess the  $\Delta CFS$  through time we find that  $\Delta CFS$  predominantly increases during mainshock  
318 rupture and remains at a high level afterwards; this is evident from our dynamic model as the  
319 normal stress change amplitude is mostly below the shear stress amplitude (Fig. 11b).

320 Temporal stress changes during the mainshock rupture also support predominantly positive  
321 shear stress changes near this creeping Garlock region (Fig. 10), whereas positive and negative  
322 normal stress distribution are observed on both sides of the projected intersection of the mainshock  
323 and Garlock fault planes (Fig. 9). Our results for temporal normal and shear stress changes near

324 the Garlock fault agree with other dynamic rupture simulations that incorporate a complex 3-D  
325 fault geometry (Lozos and Harris, 2019). Because positive normal stress changes serve to  
326 strengthen the fault whereas positive shear stresses should bring the fault closer to failure, our  
327 dynamic model offers one possible scenario that creep could have occurred as soon as ~15 seconds  
328 after nucleation of the Ridgecrest mainshock when positive shear stresses began to arrive at the  
329 Garlock fault. However, this is speculative given that we do not have information on the absolute  
330 stress state of the Garlock fault prior to the aftershock/mainshock sequence.

331 Our dynamic model suggests that the largest shear stress changes (0.3 – 0.4 MPa) arrived  
332 before and after the largest normal stress changes, but they are comparable in amplitude (Fig. 9,  
333 10, 11a). Given this maximum shear stress change amplitude, we estimate approximately 0.1  
334 centimeters of slip may have been triggered near the creeping section of the Garlock fault at a  
335 depth less than 1 km (Supplemental Fig. S5a). We also test a model where creep on the Garlock  
336 fault was exceptionally shallow (< 300 m depth; Schleicher et al., 2019) but the distribution of  
337 creep is more heterogeneous. We still obtain a similar amount of creep that is consistent with the  
338 shear stress change amplitude (Supplemental Fig. S5b). These estimates are lower than the  
339 maximum magnitude of resolved surface creep (i.e., ~3 cm) documented earlier by Barnhart et al.,  
340 (2019) and Ross et al., (2019), however. We cannot rule out the possibility that the maximum  
341 resolvable creep was driven by cumulative strain-rate changes not seen by satellite observations  
342 since the smallest observation window is at least five to six days after the mainshock (Barnhart et  
343 al., 2019). Regardless of how much triggered creep was, extensometer data imply that it did not  
344 extend very deep into the crust (Bilham and Castillo, 2020).

345 The fact that the Garlock fault did not coseismically fail is also supported by theoretical  
346 considerations to the prestress state, rupture speed and fault orientation between the mainshock  
347 and Garlock fault planes if they are connected (Poliakov et al., 2002; Kame et al., 2003). For a low  
348 angle of maximum horizontal shear stress (SH\_max) with respect to the fault (< 45 degrees), this  
349 prestress state encourages rupture to bifurcate towards the compressional side, whereas a higher  
350 angle (> 45 degrees) predicts that the rupture along the extensional side is more favorable  
351 (Poliakov et al., 2002). We use stress tensor orientations inverted by Yang and Hauksson (2013)  
352 from earthquake focal mechanisms in central and southern California to determine SH\_max. We  
353 find that the orientation of SH\_max with respect to the North near the Ridgecrest region is between  
354 zero and five degrees east of North (Fig. 1a). Given that the mainshock fault plane is approximately

355 oriented 45 degrees west of North, the SH\_max orientation with respect to the mainshock fault  
356 plane is ~50 degrees. This implies that the regional stress state would inhibit rupture propagation  
357 to the Garlock fault, since the Garlock fault is oriented along the extensional side (Fig. 1a). Our  
358 dynamic rupture model predicts an average rupture to shear-wave speed ratio of 0.4, and such low  
359 levels are not likely to encourage rupture propagation to the Garlock fault, either (Kame et al.,  
360 2003).

361 One aspect we could continue to explore in greater detail is how a fully dynamic model  
362 incorporating segmented foreshock and mainshock fault planes changes the details of the temporal  
363 stress changes on the Garlock fault. Given that the Ridgecrest sequence produced multiple  
364 orthogonal faulting with some ruptures breaking the surface while others not (Ross et al., 2019),  
365 we would expect the temporal stress change to accordingly reflect this complexity.

366 How the M6.4 foreshock and M7.1 mainshock Ridgecrest sequences changed the local  
367 stress field in Southern California is a crucial question to consider given the proximity of these  
368 events to other active faults (e.g., Garlock and San Andreas). Through a unique combination of  
369 kinematic, static, and dynamic modeling, we present a physically coherent picture of the stress  
370 changes on the central Garlock fault during and after the coseismic rupture of the M7.1 event. We  
371 find that positive stress changes near the creeping section of the Garlock fault are observed during  
372 and after coseismic rupture. We also show that the greatest shear stress change was comparable to  
373 the greatest normal stress change, but arrived earlier during dynamic rupture; this may have  
374 promoted a section of the Garlock fault to creep even before the Ridgecrest mainshock finished  
375 slipping. Our dynamic models physically explain the resolved slip amplitude through the  
376 mainshock hypocenter and reproduce the low sub-Rayleigh rupture speeds previously suggested  
377 by kinematic rupture models.

### 378 **Data and Resources**

379 Static stress calculations are conducted using the Coulomb 3 software available from the  
380 USGS website, <https://earthquake.usgs.gov/research/software/coulomb/>. All codes used in  
381 dynamic model post-processing and figure creation as well as model input and output files are  
382 archived and freely accessible on UM Deep Blue ([https:// deepblue.lib.umich.edu/](https://deepblue.lib.umich.edu/)). Seismic  
383 waveform data used in the kinematic inversion are available upon request to Dr. Shengji Wei  
384 ([shjwei@ntu.edu.sg](mailto:shjwei@ntu.edu.sg)). Some figures in this paper were generated with the Generic Mapping Tools  
385 (GMT 5, Wessel et al., 2013) or used colormap schemes from Cramer (2018).

386

387 **Acknowledgements**

388 This study was supported by the University of Michigan. M. D. Ramos and Y. Huang  
389 acknowledge the funding support by the National Science Foundation through grant award  
390 1663769.

391

392 **References**

393 Allen, C. R., Wyss, M., Brune, J. N., Grantz, A., and Wallace, R. E. (1972). Displacements on the  
394 Imperial, Superstition Hills, and San Andreas faults triggered by the Borrego Mountain  
395 earthquake, in The Borrego Mountain Earthquake of April 9, 1968. *U.S. Geol. Sur. Profess.  
396 Paper*, 787, 87-104.

397

398 Ampuero, J. P. (2009). SEM2DPACK: A spectral element method tool for 2D wave propagation  
399 and earthquake source dynamics, User's Guide, version 2.3.6. Retrieved from  
400 <http://www.sourceforge.net/projects/sem2d/>

401

402 Andrews, D. J. (1985). Dynamic plane-strain shear rupture with a slip-weakening friction law  
403 calculated by a boundary integral method. *Bull. Seismo. Soc. Of Amer.*, 75(1), 1–21.

404

405 Astiz, Luciana, Allen, C. R. (1983). Seismicity of the Garlock fault, California. *Bull. of the Seismo.  
406 Soc. of Amer.*, 73(6), 1721–1734. <https://doi.org/10.1017/CBO9781107415324.004>

407

408 Barnhart, W. D., Hayes, G. P., & Gold, R. D. (2019). The July 2019 Ridgecrest, California,  
409 Earthquake Sequence: Kinematics of Slip and Stressing in Cross-Fault Ruptures. *Geophys.  
410 Res. Lett.*, (July), 859–867. <https://doi.org/10.1029/2019GL084741>

411

412 Bilham, R., and B. Castillo (2020). The July 2019 Ridgecrest, California, Earthquake Sequence  
413 Recorded by Creepmeters: Negligible Epicentral Afterslip and Prolonged Triggered Slip  
414 at Teleseismic Distances, *Seismol. Res. Lett.* XX, 1–14, doi: 10.1785/0220190293.

415

416 Bodin, P. and Gomberg, J. (1994). Triggered Seismicity and Deformation between the Landers,  
417 California, and Little Skull Mountain, Nevada, Earthquakes. *Bulletin of the Seismological  
418 Society of America*, 84, 3, 835-843.

419

420 Brodsky, E. E., Mori, J. J., Anderson, L., Chester, F. M., Conin, M., Dunham, E. M., ... Yang, T.  
421 (2020). The State of Stress on the Fault Before, During, and After a Major Earthquake.  
422 *Annu. Rev. Earth Planet. Sci.*, 48(1), annurev-earth-053018-060507.  
423 <https://doi.org/10.1146/annurev-earth-053018-060507>

424

425 Cramer, F. (2018). Scientific colourmaps. Zenodo. <http://doi.org/10.5281/zenodo.1243862>

426

- 427 Dawson, T. E., McGill, S. F., & Rockwell, T. K. (2003). Irregular recurrence of paleoearthquakes  
428 along the central Garlock fault near El Paso Peaks, California. *Jour. of Geophys. Res: Solid*  
429 *Earth*, 108(B7). <https://doi.org/10.1029/2001jb001744>  
430
- 431 Goldberg, D. E., Melgar, D., Thomas, A., Sahakian, V. J., Xu, X., Geng, J., & Crowell, B. W.  
432 (2019, October 24). Complex Rupture of an Immature Fault Zone: A Simultaneous  
433 Kinematic Model of the 2019 Ridgecrest, CA Earthquakes.  
434 <https://doi.org/10.31223/osf.io/s79bk>  
435
- 436 Hill, M. L. and T W. Dibblee (1953). San Andreas, Garlock and Big Pine faults, California, *Bull.*  
437 *Geol Soc Am*, 64, 443-458.  
438
- 439 Ji, C., D.J. Wald, and D.V. Helmberger (2002). Source description of the 1999 Hector Mine,  
440 California earthquake; Part I: Wavelet domain inversion theory and resolution analysis,  
441 *Bull. Seism. Soc. Am.*, Vol 92, No. 4. pp. 1192-1207.  
442
- 443 Kame, N., Rice, J. R., & Dmowska, R. (2003). Effects of prestress state and rupture velocity on  
444 dynamic fault branching. *Jour. of Geophys. Res: Solid Earth*, 108(B5), 1–21.  
445 <https://doi.org/10.1029/2002jb002189>  
446
- 447 King, G. and J. Nabelek, (1985). The role of fault bends in the initiation and termination of  
448 earthquake rupture. *Science*, 228, 984-987.  
449
- 450 Lienkaemper, J. J., Galehouse, J. S., Simpson, R. W. (1997). Creep response of the Hayward fault  
451 to stress changes caused by the Loma Prieta earthquake. *Science*, 276, 5321, 2014-2016.  
452 DOI: 10.1126/science.276.5321.2014  
453
- 454 Lin, J. and R.S. Stein (2004). Stress triggering in thrust and subduction earthquakes, and stress  
455 interaction between the southern San Andreas and nearby thrust and strike-slip faults. *J. of*  
456 *Geophys. Res.*, 109, B02303, doi:10.1029/2003JB002607.  
457
- 458 Liu, C., Lay, T., Brodsky, E. E., Dascher-Cousineau, K., & Xiong, X. (2019). Coseismic Rupture  
459 Process of the Large 2019 Ridgecrest Earthquakes From Joint Inversion of Geodetic and  
460 Seismological Observations. *Geophys. Res. Lett.* <https://doi.org/10.1029/2019GL084949>  
461
- 462 Lozos, J. and Harris, R. (2019). Preliminary Dynamic Rupture Simulations of the July 2019 M6.4  
463 and M7.1 Ridgecrest, California Earthquakes, Abstract S42C-05 presented at 2019 Fall  
464 Meeting, AGU, San Francisco, CA, 9-14 Dec., 2019.  
465
- 466 Ma, S. and Archuleta, R.J., (2006). Radiated seismic energy based on dynamic rupture models of  
467 faulting, *J. Geophys. Res.*, 111, doi:10.1029/2005JB004055.  
468
- 469 Madugo, C. M., Dolan, J. F., & Hartleb, R. D. (2012). New paleoearthquake ages from the western  
470 Garlock fault: Implications for regional earthquake occurrence in Southern California. *Bull.*  
471 *of the Seismo. Soc. of Amer.*, 102(6), 2282–2299. <https://doi.org/10.1785/0120110310>  
472

- 473 McGill, S. F., and K. Sieh (1991). Surficial offsets on the central and eastern Garlock fault  
474 associated with prehistoric earthquakes, *J. Geophys. Res.*, 96, 21,597–21,621.  
475
- 476 Noda, H., and N. Lapusta (2013). Stable creeping fault segments can become destructive as a result  
477 of dynamic weakening, *Nature*, 493, 518–521, doi:10.1038/nature11703.  
478
- 479 Perrin, C., Manighetti, I., Ampuero, J.-P., Cappa, F., & Gaudemer, Y. (2016). Location of largest  
480 earthquake slip and fast rupture controlled by along-strike change in fault structural maturity  
481 due to fault growth. *Jour. of Geophys. Res: Solid Earth*, 121(5), 3666–3685.  
482 <https://doi.org/10.1002/2015JB012671>  
483
- 484 Poliakov, A. N. B., Dmowska, R., & Rice, J. R. (2002). Dynamic shear rupture interactions with  
485 fault bends and off-axis secondary faulting. *Jour. of Geophys. Res.*, 107(B11), ESE 6-1-  
486 ESE 6-18. <https://doi.org/10.1029/2001jb000572>  
487
- 488 Rice, J. R. (1992). Fault Stress States, Pore Pressure Distributions, and the Weakness of the San  
489 Andreas Fault. *Inter. Geophys.*, 51(C), 475–503. [https://doi.org/10.1016/S0074-  
490 6142\(08\)62835-1](https://doi.org/10.1016/S0074-6142(08)62835-1)  
491
- 492 Ripperger, J., & Mai, P. M. (2004). Fast computation of static stress changes on 2D faults from  
493 final slip distributions. *Geophys. Res. Lett.*, 31(18), 2–5.  
494 <https://doi.org/10.1029/2004GL020594>  
495
- 496 Ross, Z. E., Idini, B., Jia, Z., Stephenson, O. L., Zhong, M., Wang, X., ... Moore, A. W. (2019).  
497 2019 Ridgecrest earthquake sequence. *Science*, 3665(October), 346–351.  
498
- 499 Schleicher, L. S., Huang, M., Allison, K. L., and Anderson, R. J. (2019). Seismic hazard  
500 implications of post-seismic deformation and stress transfer from the 2019 Searles Valley  
501 California Earthquakes, Abstract S41C-08 presented at 2019 Fall Meeting, AGU, San  
502 Francisco, CA, 9-14 Dec., 2019.  
503
- 504 Toda, S., R. S. Stein, K. Richards-Dinger and S. Bozkurt (2005). Forecasting the evolution of  
505 seismicity in southern California: Animations built on earthquake stress transfer. *J.*  
506 *Geophys. Res.*, 110, B05S16, doi:10.1029/2004JB003415.  
507
- 508 Tinti, E., Cocco, M., Fukuyama, E., & Piatanesi, A. (2009). Dependence of slip weakening  
509 distance ( $D_c$ ) on final slip during dynamic rupture of earthquakes. *Geophys. Jour. Int.*,  
510 177(3), 1205–1220. <https://doi.org/10.1111/j.1365-246X.2009.04143.x>  
511
- 512 Wessel, P., W. H. F. Smith, R. Scharroo, J. F. Luis, and F. Wobbe, Generic Mapping Tools:  
513 Improved version released, *EOS Trans. AGU*, 94, 409-410, 2013.  
514
- 515 Xu, X., D. T. Sandwell, and B. Smith-Konter (2020). Coseismic Displacements and Surface  
516 Fractures from Sentinel-1 InSAR: 2019 Ridgecrest Earthquakes, *Seismol. Res. Lett.* XX,1–  
517 7, doi: 10.1785/ 0220190275.  
518

519 Yang, W. and Hauksson, E., (2013). The tectonic crustal stress field and style of faulting along the  
520 Pacific North America Plate boundary in Southern California, *Geophys. Jour. Int.*, 194, 100-  
521 117, doi: 10.1093/gji/ggt113

522 **Author Mailing Addresses**

- 523 1. Marlon D. Ramos, Jing Ci Neo, Prithvi Thakur, Yihe Huang  
524 2. Shengji Wei

525

526 Authors one through four may be contacted at:

527

528 Department of Earth and Environmental Sciences

529 University of Michigan

530 Room 2534

531 Attn: Marlon D. Ramos, Jing Ci Neo, Prithvi Thakur, Yihe Huang

532 1100 North University Avenue

533 Ann Arbor, MI 48109-1005

534 Author five may be contacted at:

535

536 Earth Observatory of Singapore

537 Nanyang Technological University

538 Attn: Wei Shengji

539 N2-01A-08

540 50 Nanyang Ave, Singapore 639798

541

542

543

544

545

546

547

548

549

550

551

Preprint submitted to EarthArXiv



552 **List of Tables**

553

554

555

**Table 1**

556 Coulomb stress-change parameters of the mainshock and aftershock fault planes. Hypocenter  
557 location (latitude, longitude, depth) and maximum slip amplitude (meters) from kinematic  
558 inversion are also listed.

559

	<b>M<sub>w</sub></b>	<b>Hypocenter</b>	<b>Strike</b>	<b>Dip</b>	<b>Rake</b>	<b>Peak Slip (m)</b>
<b>Mainshock</b>	7.1	35.772N -117.602E 3 km	322	81	-170	4.7
<b>Foreshock</b>	6.4	35.705N -117.506E 9 km	318 228	88 81	-172 0	1.3 0.74

560

561

562

563

564

565

566

567

568

569

570

571

572

573

574

575

576

577

578

579

580

Preprint submitted to EarthArXiv

581 **List of Figure Captions**

582

583 **Figure 1.** 2019 Ridgecrest Sequence. A) Dynamic rupture model framework in a compressive  
584 stress field. The mainshock is modeled as a mode II shear-crack that is  $\sim 110$  degrees (clockwise)  
585 from the Garlock fault. Whether rupture will branch from the mainshock to Garlock fault is  
586 determined by the rupture speed ( $v_r$ ), prestress level on the fault, and maximum compressional  
587 stress direction (SH\_max). B) Study area with foreshock-mainshock focal mechanism solutions  
588 (USGS) and the western, central, and eastern Garlock fault segments. Yellow box denotes  
589 approximate location of geodetically imaged fault creep. SH\_max field from Yang and Hauksson  
590 (2013). SAF = San Andreas Fault.

591

592 **Figure 2.** Ridgecrest slip inversion results obtained using teleseismic and local strong-motion data.  
593 The mainshock fault is 100 km long, with foreshock fault plane 1 and foreshock plane 2 indicated.  
594 The black line denotes the surface trace of the Garlock fault.

595

596 **Figure 3.** Mainshock slip inversion results.

597

598 **Figure 4.** Coulomb stress change due to foreshock plane 1 and 2 on the mainshock fault plane  
599 calculated at a depth of 5 km and with a friction coefficient of 0.6. A) The combined effect of slip  
600 on the mainshock and both aftershock fault planes. B) The Coulomb stress change from plane 1  
601 which is parallel to the main fault plane. C) Coulomb stress change from plane 2, which is the NE-  
602 SW striking cross-fault. The aftershocks depicted are the earthquakes that occurred after the  
603 foreshock and do not include those induced from mainshock stress changes.

604

605 **Figure 5.** Coulomb stress change of the mainshock on a receiver fault of  $70^\circ$  strike and  $90^\circ$  dip,  
606 approximating the leftmost part of the Garlock fault in this figure. Top: Coulomb stress-change  
607 results for a 5 km depth source at friction coefficients of 0.2, 0.4, and 0.6. Bottom: Coulomb stress-  
608 change results for a 10 km depth source with the same friction coefficients.

609

610 **Figure 6.** Static stress-drop (top) and initial shear stress (bottom) along the mainshock fault  
611 plane. Static stress-drop is calculated assuming a homogeneous, Poisson medium and initial  
612 shear stress is computed using the complete stress-drop assumption. We select an initial shear  
613 stress profile through the main asperity at 3 km depth (dashed black line) as a starting condition  
614 for our 2-D dynamic rupture models.

615

616 **Figure 7.** A) Along-fault slip distribution resolved by the kinematic slip inversion (black line)  
617 and that calculated from the dynamic rupture model (dashed blue line). The earthquake is nucleated  
618 at (0,0) as indicated by the magenta star. B) Dynamic stress-drop along the fault. Location shown  
619 in Figure 6. C) Spatiotemporal and bilateral rupture history predicted by the dynamic rupture  
620 model. Colorbar denotes slip-rate and the slope of the gradient between zero and peak slip-rate  
621 signifies the rupture front speed (solid white lines). Both rupture fronts propagate at sub-Rayleigh  
622 wave speed.

623

624

625 **Figure 8.** Static stress-change field in the modeling domain rotated to the strike of the Garlock  
626 fault. A) normal stress and B) shear stress. Garlock fault trace (dashed black line) and Ridgecrest  
627 mainshock fault (bold black line) are superimposed onto the figure. Yellow box denotes  
628 approximate location of the creeping region (Barnhart et al., 2019).  
629

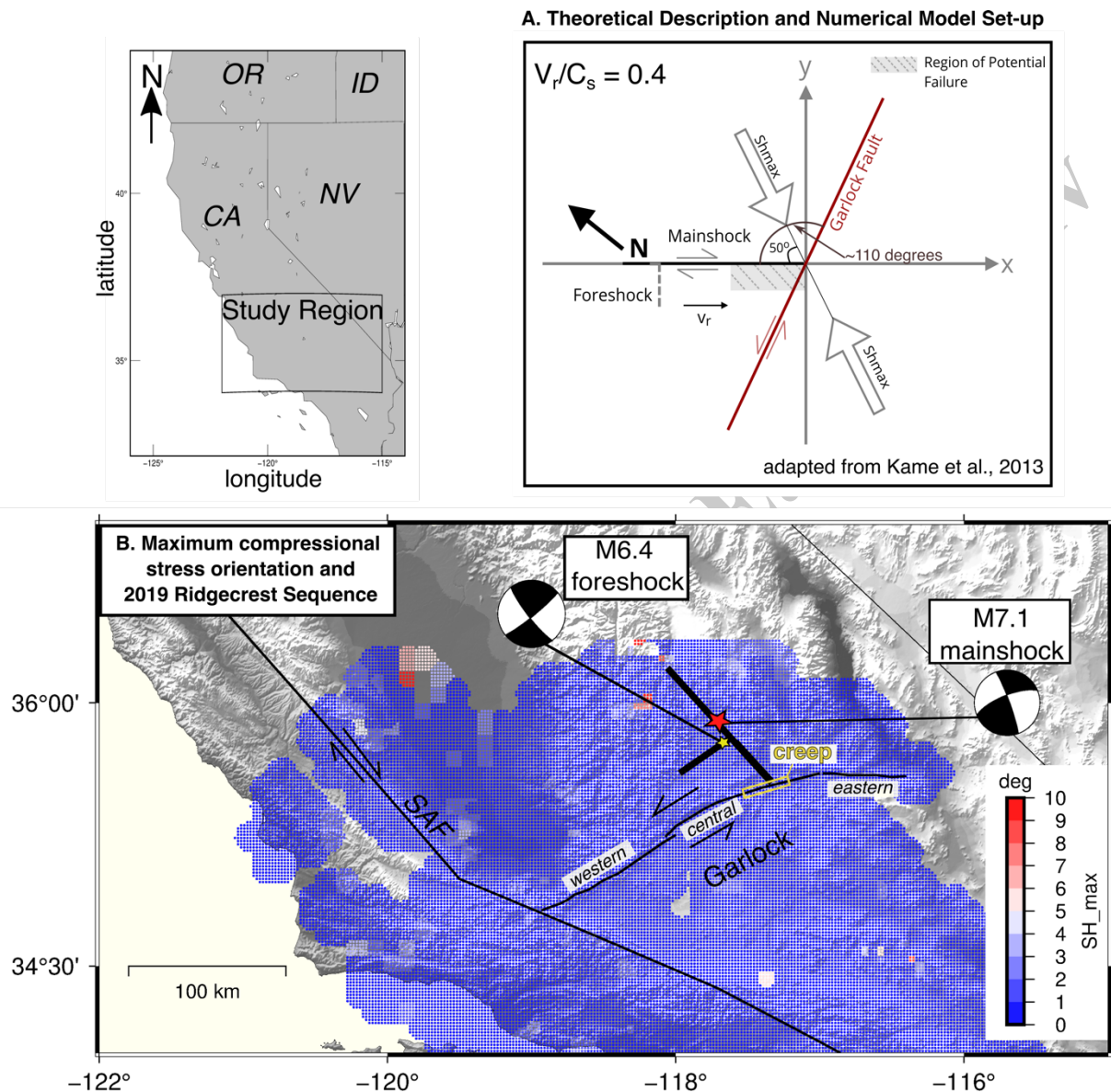
630 **Figure 9.** Normal stress changes ( $\sigma_{yy}$ ) at various moments in time on the central Garlock fault  
631 during coseismic rupture of the mainshock. A point on the Garlock (-10km, -60 km) is selected  
632 to visualize the stress amplitude variability (yellow dot). Subfigures A through E represent  $\sigma_{yy}$   
633 from 17.5 to 50 during rupture propagation. Subfigure F shows the time-history of  $\sigma_{yy}$  where the  
634 blue squares denote the amplitude change at each of the normal stress snapshots (A-E). GF =  
635 Garlock fault.  
636

637 **Figure 10.** Similar to Fig. 9, but shear stress changes ( $\sigma_{xy}$ ) during coseismic rupture.  $\sigma_{xy}$  exhibits  
638 three distinct peaks in its temporal stress-change on the Garlock fault at ~28, 38, and 50 seconds.  
639

640 **Figure 11.** Stress change evolution on a section of the Garlock fault during the entire Ridgecrest  
641 simulation. A) Normal and shear stress change. B) Coulomb stress change for various friction  
642 coefficients assessed in the static stress change analysis. Note that we plot the temporal stress  
643 change starting at 10 seconds because this is when the nucleation procedure ceases.  
644

645  
646  
647  
648  
649  
650  
651  
652  
653  
654  
655  
656  
657  
658  
659  
660  
661  
662  
663  
664  
665  
666  
667  
668  
669

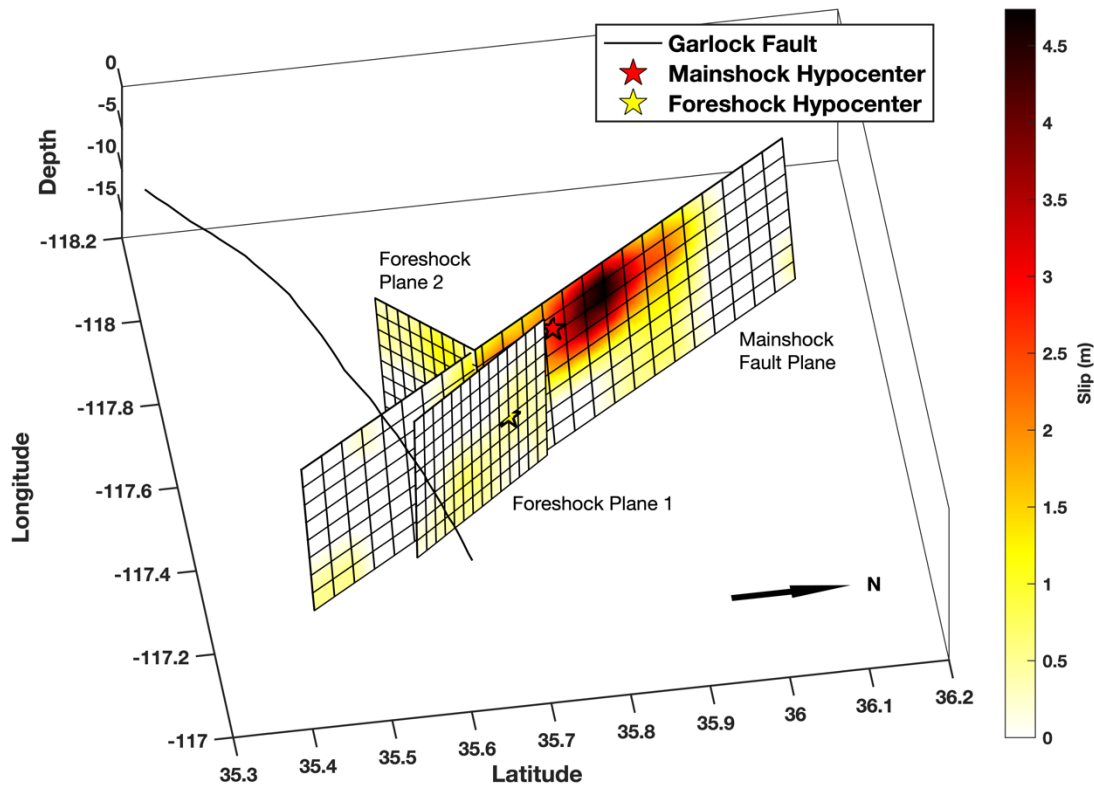
670  
 671 **Figures**  
 672



673  
 674 **Figure 1.** 2019 Ridgecrest Sequence. A) Dynamic rupture model framework in a compressive  
 675 stress field. The mainshock is modeled as a mode II shear-crack that is ~110 degrees (clockwise)  
 676 from the Garlock fault. Whether rupture will branch from the mainshock to Garlock fault is  
 677 determined by the rupture speed ( $v_r$ ), prestress level on the fault, and maximum compressional  
 678 stress direction (SH<sub>max</sub>). B) Study area with foreshock-mainshock focal mechanism solutions  
 679 (USGS) and the western, central, and eastern Garlock fault segments. Yellow box denotes  
 680 approximate location of geodetically imaged fault creep. SH<sub>max</sub> field from Yang and Hauksson  
 681 (2013). SAF = San Andreas Fault.

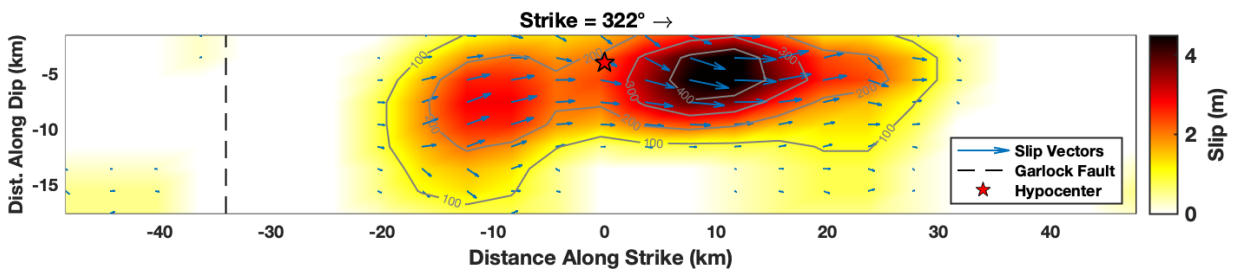
682  
 683

684  
685



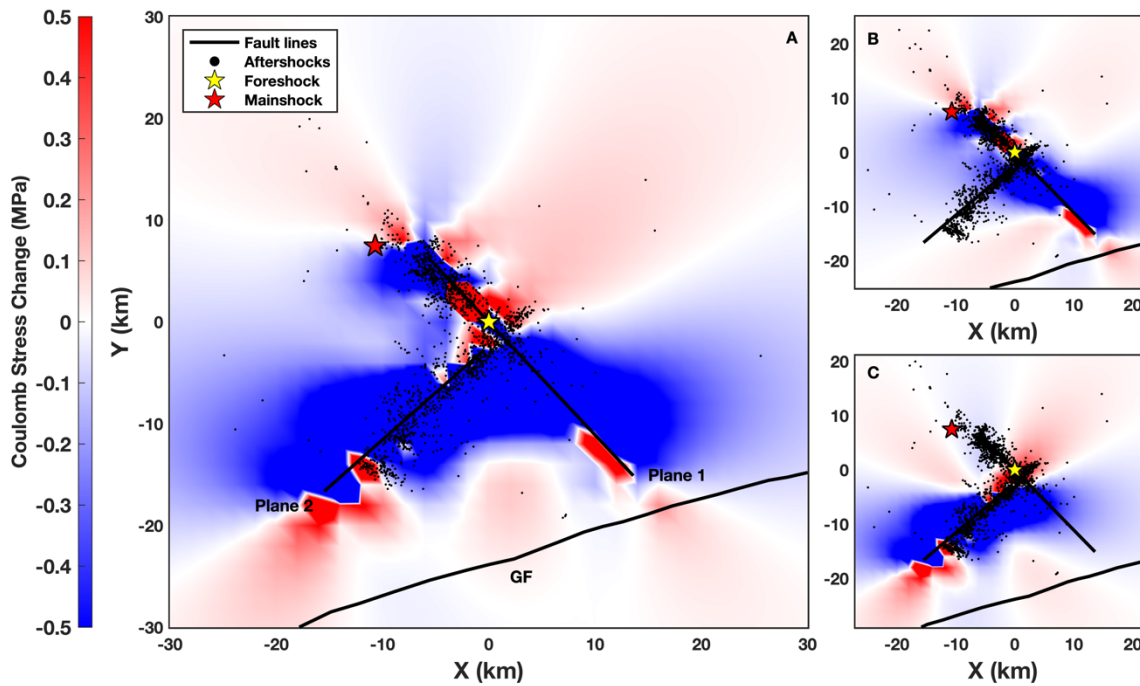
686  
687  
688  
689  
690  
691

**Figure 2.** Ridgecrest slip inversion results obtained using teleseismic and local strong-motion data. The mainshock fault is 100 km long, with foreshock fault plane 1 and foreshock plane 2 indicated. The black line denotes the surface trace of the Garlock fault.



692  
693  
694  
695  
696

**Figure 3.** Mainshock slip inversion results.



697  
698 **Figure 4.** Coulomb stress change due to foreshock plane 1 and 2 on the mainshock fault plane  
699 calculated at a depth of 5 km and with a friction coefficient of 0.6. A) The combined effect of slip  
700 on the mainshock and both aftershock fault planes. B) The Coulomb stress change from plane 1  
701 which is parallel to the main fault plane. C) Coulomb stress change from plane 2, which is the NE-  
702 SW striking cross-fault. The aftershocks depicted are the earthquakes that occurred after the  
703 foreshock and do not include those induced from mainshock stress changes.

704  
705  
706

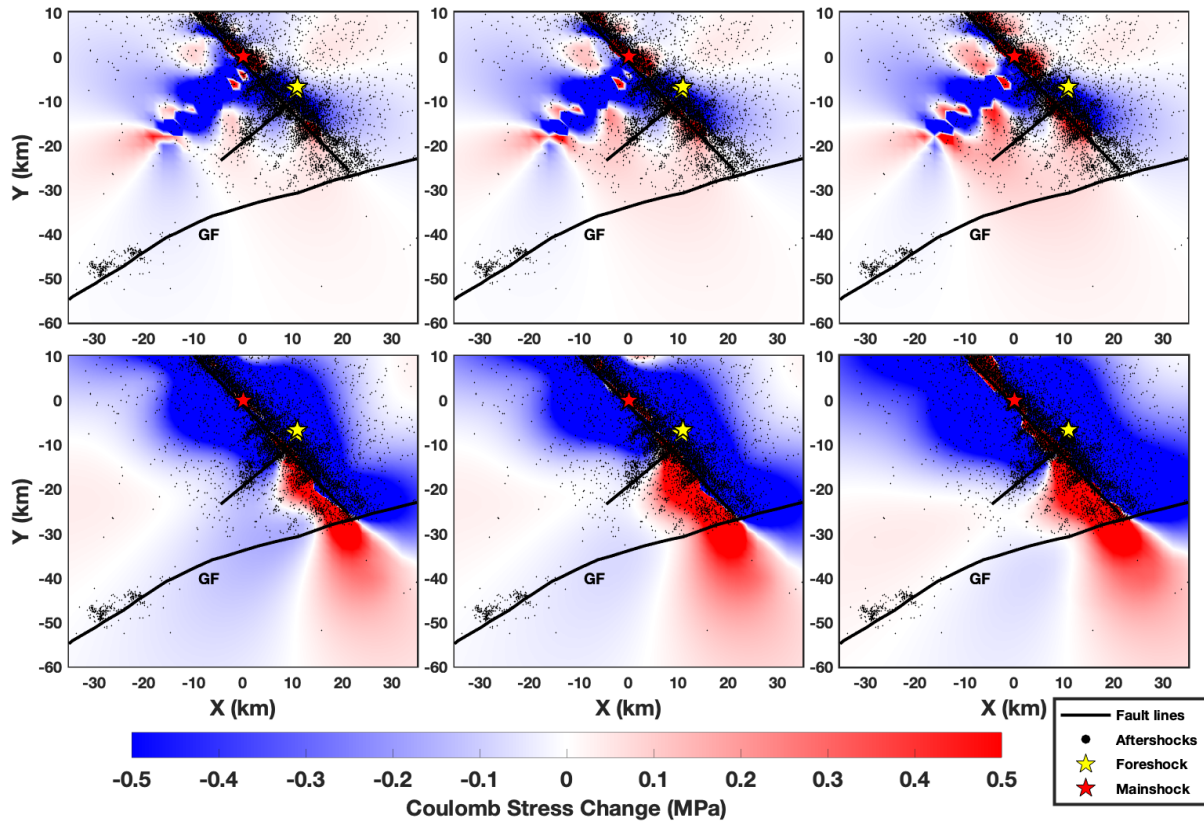
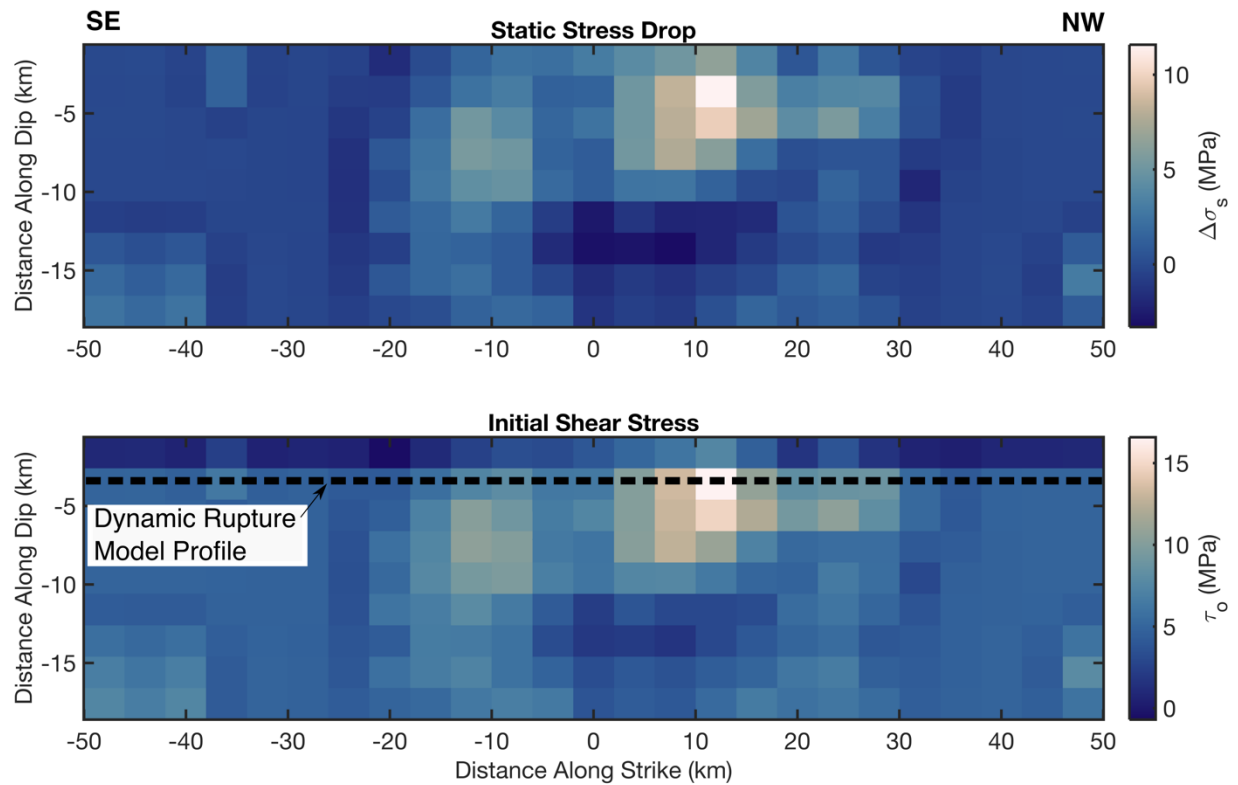


**Figure 5.** Coulomb stress change of the mainshock on a receiver fault of  $70^\circ$  strike and  $90^\circ$  dip, approximating the leftmost part of the Garlock fault in this figure. Top: Coulomb stress-change results for a 5 km depth source at friction coefficients of 0.2, 0.4, and 0.6. Bottom: Coulomb stress-change results for a 10 km depth source with the same friction coefficients.

707  
 708  
 709  
 710  
 711  
 712  
 713  
 714  
 715  
 716  
 717  
 718  
 719  
 720  
 721  
 722  
 723  
 724  
 725  
 726  
 727  
 728  
 729  
 730

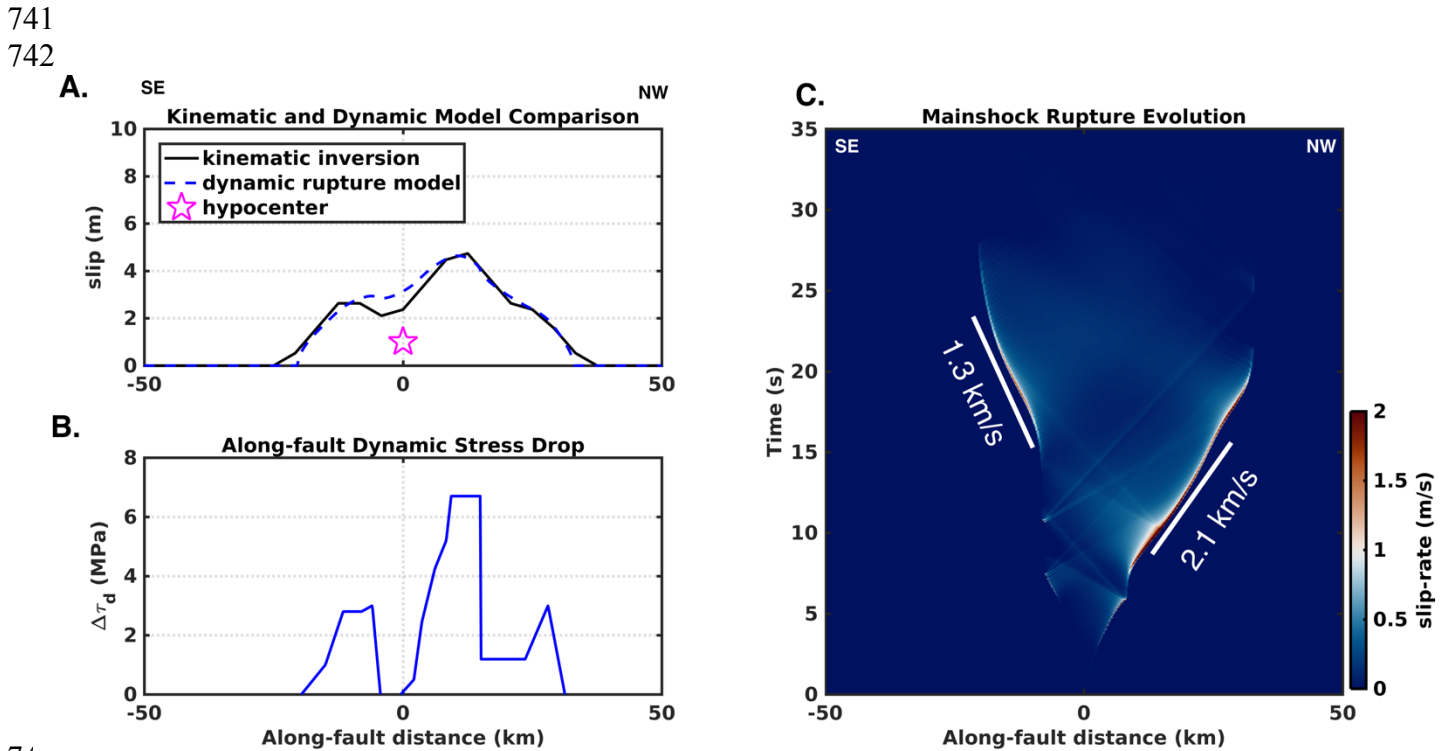
731  
732



733  
734 **Figure 6.** Static stress-drop (top) and initial shear stress (bottom) along the mainshock fault plane.  
735 Static stress-drop is calculated assuming a homogeneous, Poisson medium and initial shear stress  
736 is computed using the complete stress-drop assumption. We select an initial shear stress profile  
737 through the main asperity at 3 km depth (dashed black line) as a starting condition for our 2-D  
738 dynamic rupture models.

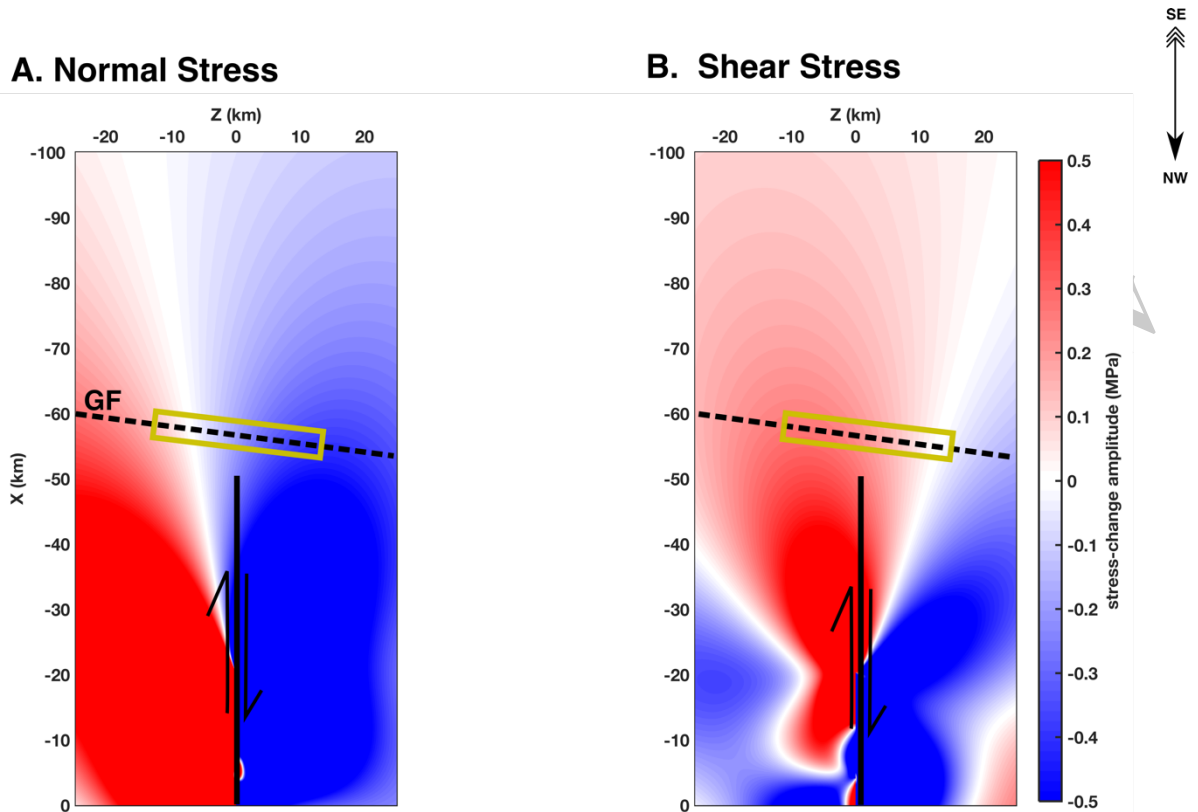
739  
740





743  
744 **Figure 7.** A) Along-fault slip distribution resolved by the kinematic slip inversion (black line)  
745 and that calculated from the dynamic rupture model (dashed blue line). The earthquake is nucleated  
746 at (0,0) as indicated by the magenta star. B) Dynamic stress-drop along the fault. Location shown  
747 in Figure 6. C) Spatiotemporal and bilateral rupture history predicted by the dynamic rupture  
748 model. Colorbar denotes slip-rate and the slope of the gradient between zero and peak slip-rate  
749 signifies the rupture front speed (solid white lines). Both rupture fronts propagate at sub-Rayleigh  
750 wave speed.

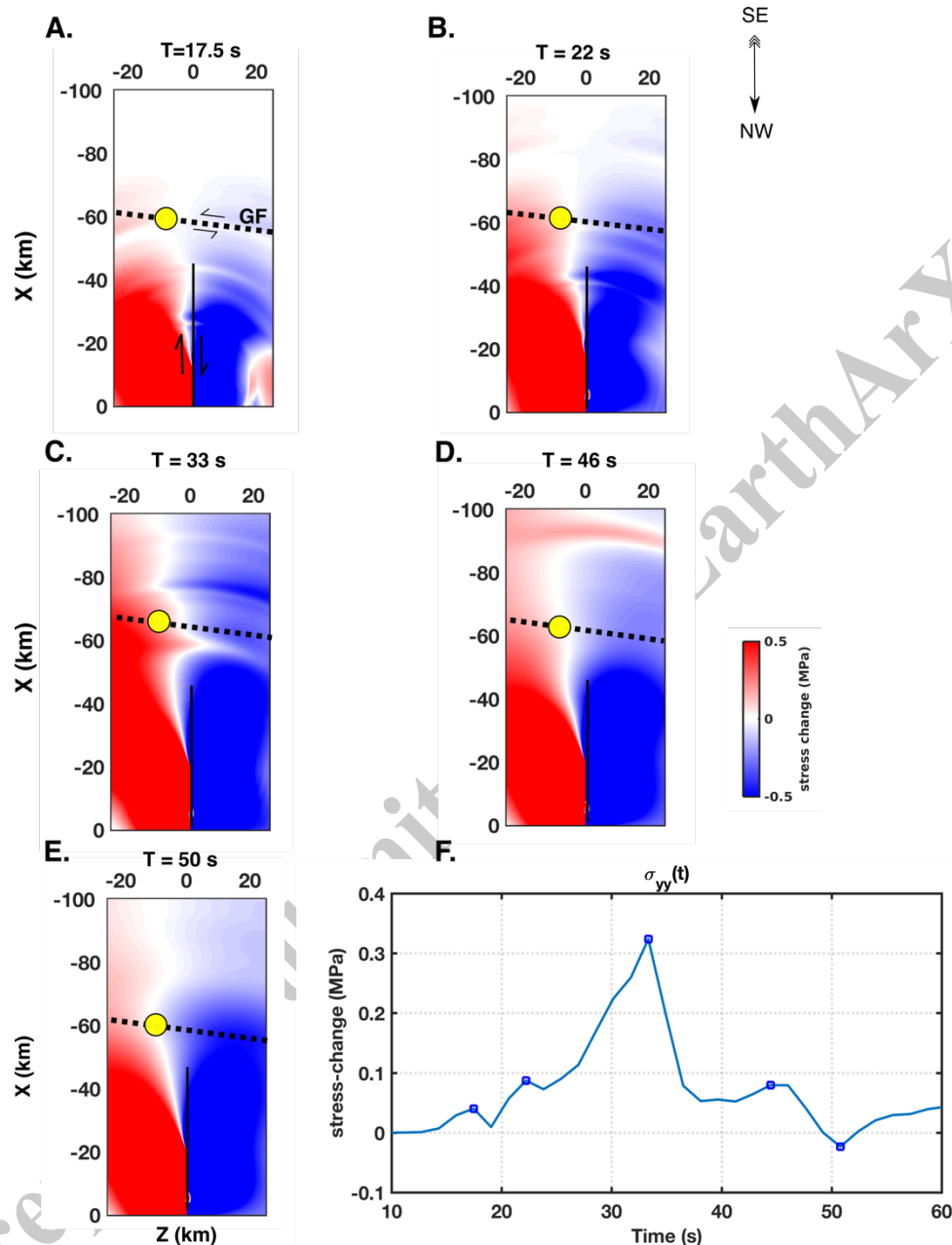
751  
752  
753  
754  
755



756  
757  
758  
759  
760  
761  
762  
763  
764  
765  
766  
767  
768  
769  
770  
771  
772  
773  
774  
775  
776  
777  
778  
779

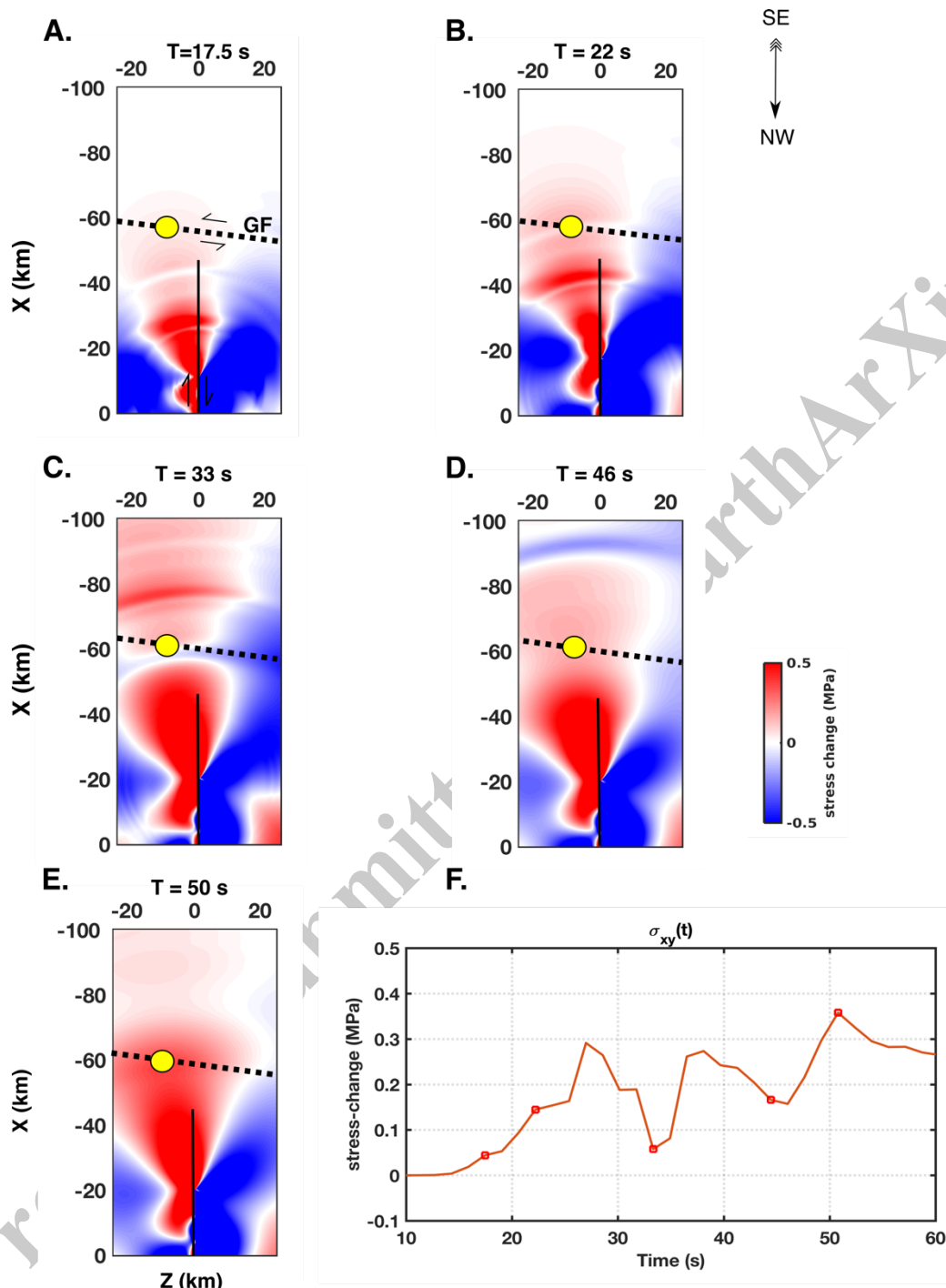
**Figure 8.** Static stress-change field in the modeling domain rotated to the strike of the Garlock fault. A) normal stress and B) shear stress. Garlock fault trace (dashed black line) and Ridgecrest mainshock fault (bold black line) are superimposed onto the figure. Yellow box denotes approximate location of the creeping region (Barnhart et al., 2019).

780  
 781



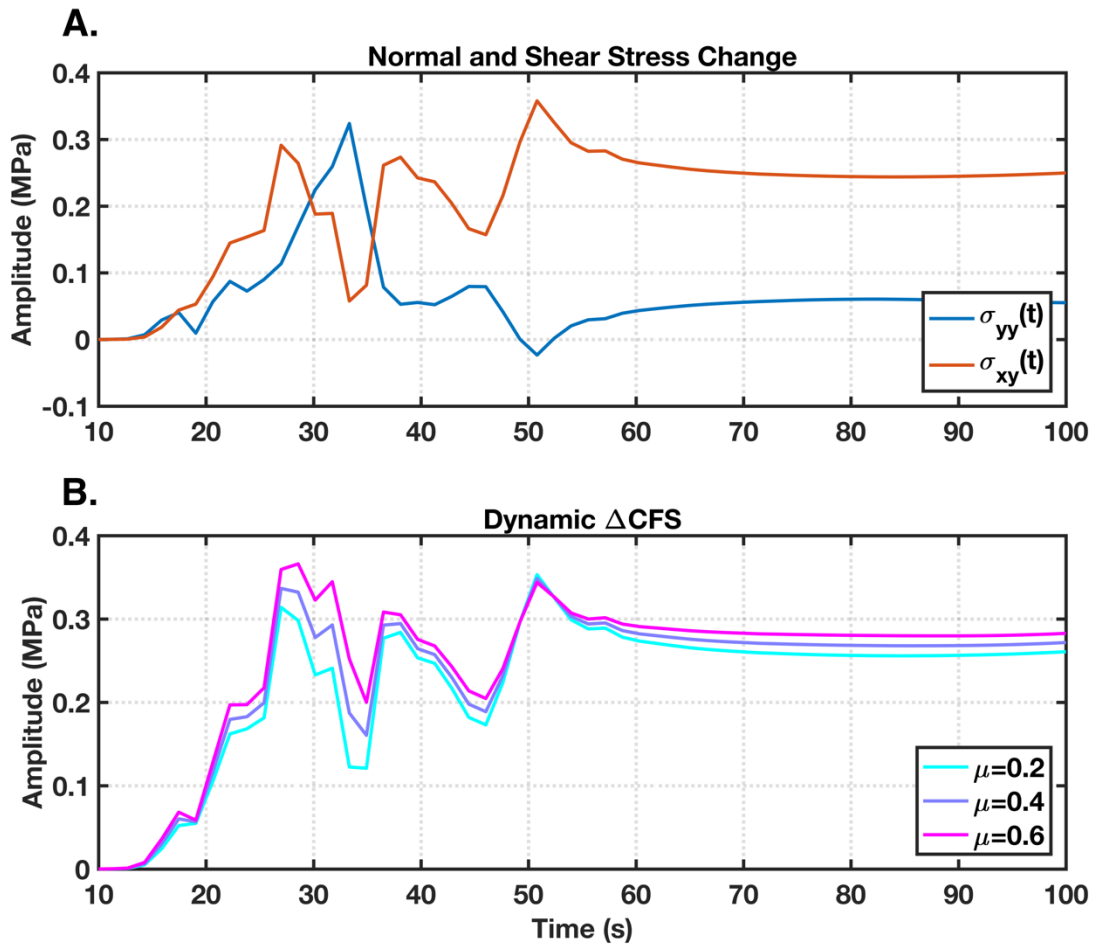
782  
 783  
 784  
 785  
 786  
 787  
 788  
 789

**Figure 9.** Normal stress changes ( $\sigma_{yy}$ ) at various moments in time on the central Garlock fault during coseismic rupture of the mainshock. A point on the Garlock (-10km, -60 km) is selected to visualize the stress amplitude variability (yellow dot). Subfigures A through E represent  $\sigma_{yy}$  from 17.5 to 50 seconds during rupture propagation. Subfigure F shows the time-history of  $\sigma_{yy}$  where the blue squares denote the amplitude change at each of the normal stress snapshots (A-E).



790  
 791 **Figure 10.** Similar to Fig. 9, but shear stress changes ( $\sigma_{xy}$ ) during coseismic rupture.  $\sigma_{xy}$  exhibits  
 792 three distinct peaks in its temporal stress-change on the Garlock fault at  $\sim 28$ , 38, and 50 seconds.  
 793  
 794  
 795  
 796  
 797

798  
799



800  
801 **Figure 11.** Stress change evolution on a section of the Garlock fault during the entire Ridgecrest  
802 simulation. A) Normal and shear stress change. B) Coulomb stress change for various friction  
803 coefficients assessed in the static stress change analysis. Note that we plot the temporal stress  
804 change starting at 10 seconds because this is when the nucleation procedure ceases.